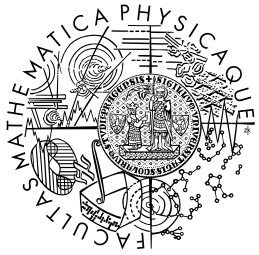

FACULTY
OF MATHEMATICS
AND PHYSICS
Charles University

MASTER THESIS

Lea Uhliarová

Tile Calorimeter test beam data analysis

Institute of Particle and Nuclear Physics

Supervisor of the thesis:	doc. RNDr. Tomáš Davídek, Ph.D.
Study programme:	Physics
Study branch:	Nuclear and subnuclear physics

Prague 2020

I declare that I carried out this thesis independently, and only with the cited sources, literature and other professional sources.

I understand that my work relates to the rights and obligations under the Act No. 121/2000 Sb., the Copyright Act, as amended, in particular the fact that the Charles University has the right to conclude a license agreement on the use of this work as a school work pursuant to Section 60 subsection 1 of the Copyright Act.

In ..... date ..... signature of the author

I would like to express my gratitude to my supervisor doc. RNDr. Tomáš Davídek, Ph.D. for the guidance throughout this thesis, for valuable insights and patience. I am also grateful to Stanislav Poláček for his advice and to my family and close ones for support.

Title: Tile Calorimeter test beam data analysis

Author: Lea Uhliarová

Institute: Institute of Particle and Nuclear Physics

Supervisor: doc. RNDr. Tomáš Davídek, Ph.D., Institute of Particle and Nuclear Physics

Abstract:

Tile Calorimeter modules are regularly tested in the CERN SPS North Area, as they are an integral part of the ATLAS experiment at the Large Hadron Collider at CERN. In this thesis, test beam data from November 2018 were used for two separate analyses.

Muon SPS H8 beam allowed for the review of radial electromagnetic calibration in the extended barrel module EBC65. Data from November 2018 test beam confirmed the correctness of previously established and used constants for rectifying uneven response in A, BC and D cell rows.

In the second analysis, hadron beam from the SPS accelerator impinging on the Tile Calorimeter modules in the projective geometry was utilized. It served to determine the distribution of the mean energy in the calorimeter for hadronic showers in Tile Calorimeter at η varying from -0.05 up to -0.65.

Keywords: ATLAS, Tile Calorimeter, test beam, muons, pions

Contents

Introduction

European Organization for Nuclear Research, known as CERN, was established in 1953 [1] to push the limits of fundamental nuclear research. CERN currently comprises 23 member states contributing to the research of nuclear and particle physics, as well as innovating technology on the way.

Large Hadron Collider (LHC) is a 27 kilometers-long ring designed for accelerating protons up to the energy of 7 TeV. Currently, the maximal reached energy is 6,5 TeV. The 4 largest experiments at CERN - ATLAS, CMS, LHCb, ALICE - explore the laws of physics by colliding protons from the LHC. Accelerated protons are colliding in the experiments attaining the total collision energy of 13 TeV and instantaneous luminosity of $5 \cdot 10^{34}\,\mathrm{cm}^{-2}\mathrm{s}^{-1}$. Currently, the LHC and all the experiments are shut down with a planned return into operation in May 2021 for the beginning of Run 3 [2].

Placed on the circumference of LHC, ATLAS is the largest detector at CERN. It aims to discover new particles, as well as, to get more precise measurements of the particles that have already been discovered. ATLAS, together with CMS, shares the credit, e.g. for the Higgs boson discovery in 2012 [3] and the precision measurements of its characteristics ongoing since it was discovered.

In this paper, we are going to focus on test beam data. More specifically, we are going to study the response of the ATLAS hadronic calorimeter to muon and pion beams.

1. ATLAS experiment

ATLAS (in figure 1.1) was designed to serve as a laboratory for a broad range of measurements in particle physics. Since its construction, it was used for detecting new particles, such as the Higgs boson [3], and also for more precise measurements of previously known particles and processes they participate in.

Bunches of protons accelerated in the LHC are colliding in the so-called interaction point at the center of ATLAS with the total energy of 13 TeV. Around the collision point, several layers of detectors are detecting the paths, momenta, and energies of particles emerging from the collision. The inner detector is the closest to the interaction point, followed by calorimeters and muon chambers. A system of 2 T and 4 T magnets, placed around the detectors, complements the detector system, and bends particle's trajectory and therefore enables the momentum measurement.

The trigger system of ATLAS ensures the choice of the scientifically interesting events and sends these to the Data Acquisition System for further manipulation and storage.

1.1 Inner detector

The Inner detector is recording the characteristics (path, momentum, and charge) of electrically charged particles. Pixel detector, semiconductor tracker, and transition radiation tracker together form the inner detector, and they are all enfolded in a magnetic field of 2 T.

Since the Inner detector is the closest one to the interaction point, its components have to be considerably radiation-resistant.

1.2 Calorimeters

Calorimeters are measuring the energy and the direction of the traversing particles. Calorimeters can determine these characteristics for most of neutral and charged particles. Jets and showers of particles need to be completely absorbed in the body of the calorimeter to correctly detect the energy of the particles. Therefore, the length of the calorimeter is one of the decisive parameters.

There are two calorimeter types (see figure 1.2) among ATLAS detectors:

- Liquid Argon (LAr) Calorimeter - forward calorimeter, electromagnetic calorimeter and hadronic endcaps
- Tile Calorimeter (TileCal) - hadronic calorimeter

Both of them have a sandwich structure, meaning there is a passive layer (allowing the shower of particles to expand) and an active layer (recording the energy of the shower through sending the signal to photomultipliers). In this thesis, we are interested further in the hadronic calorimeter.

Hadronic calorimeter TileCal is a part of the ATLAS detector system placed right between Electromagnetic calorimeter and Muon spectrometer. Its inner radius is 2.28 m and the outer one is 4.23 m [6]. TileCal has 3 main parts. Central

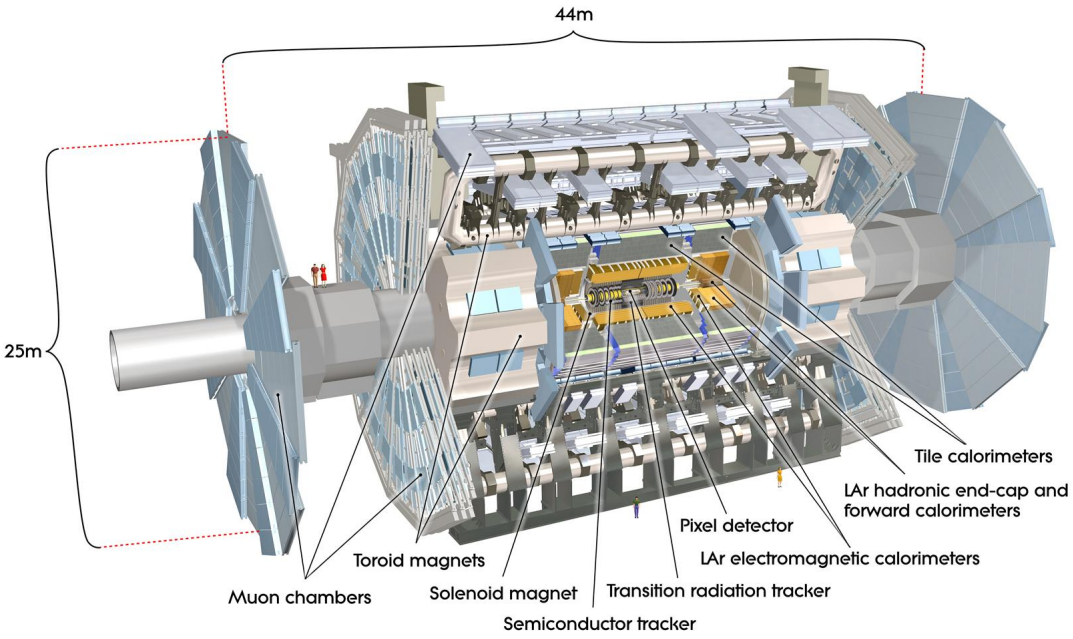

Figure 1.1: ATLAS experiment in CERN [4].

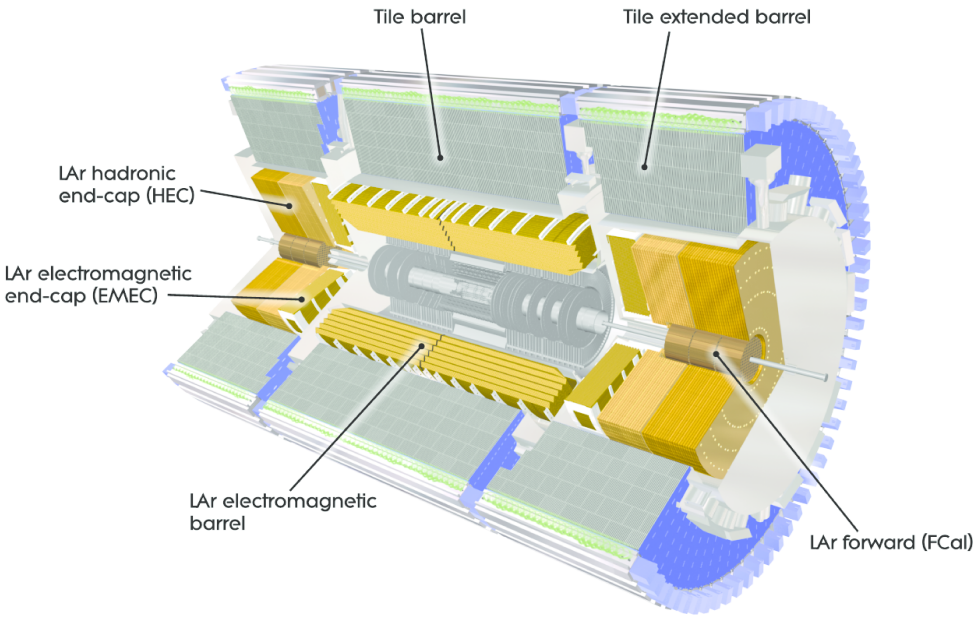

Figure 1.2: Electromagnetic and hadronic calorimeters [5].

barrel and two extended barrels at the ends of the ATLAS detector. Both central and extended barrels consist of 64 modules like the one in figure 2.1. Modules are placed azimuthally around the beam axis, covering a 2π angle.

1.3 Muon spectrometer

Similarly to the Inner detector, Muon spectrometer needs to be enfolded in a magnetic field to be able to measure the momenta of the particles. The magnetic field for the Muon spectrometer is supplied by 4 T Barrel Toroid and 4 T Endcap Toroids.

By the time particles get to the Muon spectrometer, which is the most distant ATLAS detector from the collision point, the majority of the particles have already been absorbed in the inner detector or calorimeters. Muons and neutrinos are the only known particles not absorbed by the previous detector layers. Moreover, neutrinos are not interacting in the muon chambers, so the only particles detected at this level are muons, as the name 'Muon spectrometer' suggests.

Muon spectrometer is composed out of several chamber types. MDT (Monitored Drift Tubes) and CSC (Cathode Strip Chambers) guarantee the accurate measurement of the muon coordinates and trajectory curvatures. TGC (Thin Gas Chambers) and RPC (Resistive Plate Chambers) take care of triggering and the second coordinate measurement.

2. Tile hadronic calorimeter

Hadronic calorimeter detects the energy and direction of incoming hadron particles, such as protons, neutrons, Λ^0, pions, kaons or B^0 mesons. The measurement is based on the process of hadron interaction with matter. When charged or neutral hadrons enter a hadronic calorimeter they interact with its material and create showers of new particles. All of the emerging particles need to be absorbed in the body of the calorimeter. Then, not only the direction but also the energy of particles can be measured precisely.

As muons are interacting with the calorimeter through ionization, we can also detect muons at the TileCal level. This allows TileCal to assist muon measurements and complement data needed for the determination of muon energy and its trajectory direction, if needed. Muon energy and direction is reconstructed mainly through Inner detector and Muon spectrometer measurements.

2.1 Composition

To ensure the measurement of the energy and the direction of hadrons TileCal has a sandwich structure. The sandwich structure indicates that alternating active and passive layers form the body of the calorimeter. The sandwich-like structure is created by laying steel plates and scintillation tiles one onto another (see figure 2.1), their shorter side facing the interaction point at the heart of the ATLAS detector.

In figure 2.1, there is one module of TileCal displayed. Looking at the module, we see its mechanical composition. The alternating plates and tiles are grouped into 11 tile rows from the bottom to the top of the displayed module. The 11 tile rows are organized radially with respect to the detector geometry. Tile row 1 (at the bottom in figure 2.1) is the closest to the interaction point. The furthest from the interaction point is tile row 11, which is composed of the largest plates and tiles when comparing to the rest of the tile rows.

2.2 Calibration

Before recording TileCal data in ATLAS experiment, TileCal modules need to be properly calibrated. Calibration is achieved in several steps:

- Charge injection system
- Laser calibration
- Minimum bias system
- Radioactive source
- Time calibration
- Electromagnetic calibration

In chapter 4, we will delve more into electromagnetic calibration.

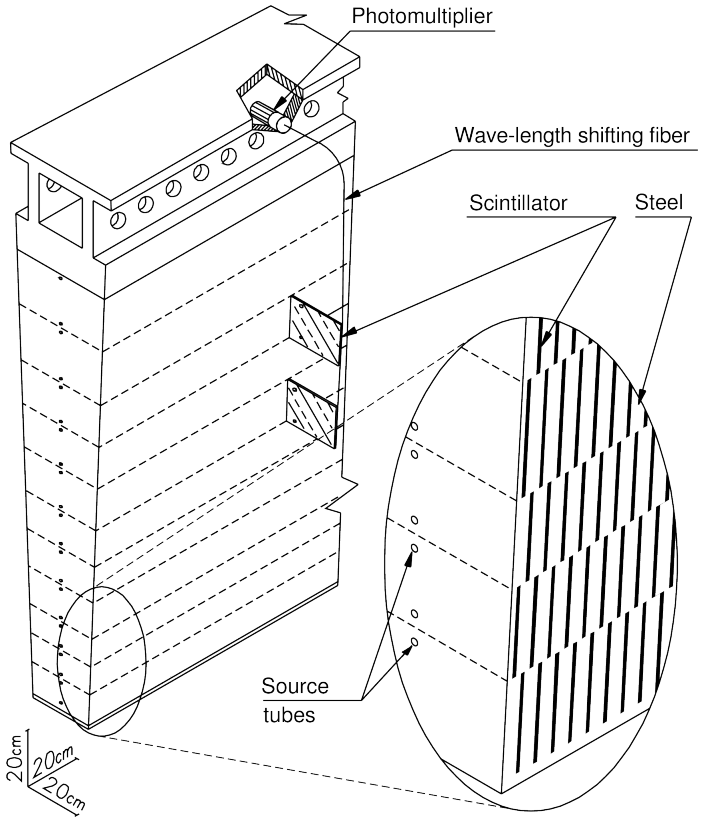

Figure 2.1: Tile composition of TileCal [5].

2.3 Readout

Firstly, the hadronic shower develops in the passive layer from steel plates. Afterwards, the signal emitted from the shower is recorded in the active layer represented by plastic scintillation tiles. As shown in figure 2.1, the signal from both sides of each scintillation tile is conducted via wavelength-shifting optical fibres to PMTs (photomultipliers). These, in turn, convert the optical signal to an electrical signal, which is sent through several levels of trigger system for sorting. In the end, chosen events are kept in a storage system.

For readout purposes, we divide each module into readout cells. A cell is formed by a group of tiles read out by optical fibres leading to two PMTs. One PMT reads out the signal from the left side of the cell and the other one from the right side. The total signal from one cell is then the sum of the signal from two PMTs corresponding to the cell. Mapping of cells (see figure 2.2) for the central barrel compared to extended barrel modules is slightly different. One cell row includes several tile rows (see figure 2.1). The number of tile rows comprised in one cell row differs between the central barrel and extended barrel module.

Trigger system

When PMT receives the optical signal from a grouping of wavelength-shifting fibres corresponding to one side of a cell, the signal is shaped to a constant width and then it is divided into two gain branches - high and low. The am-

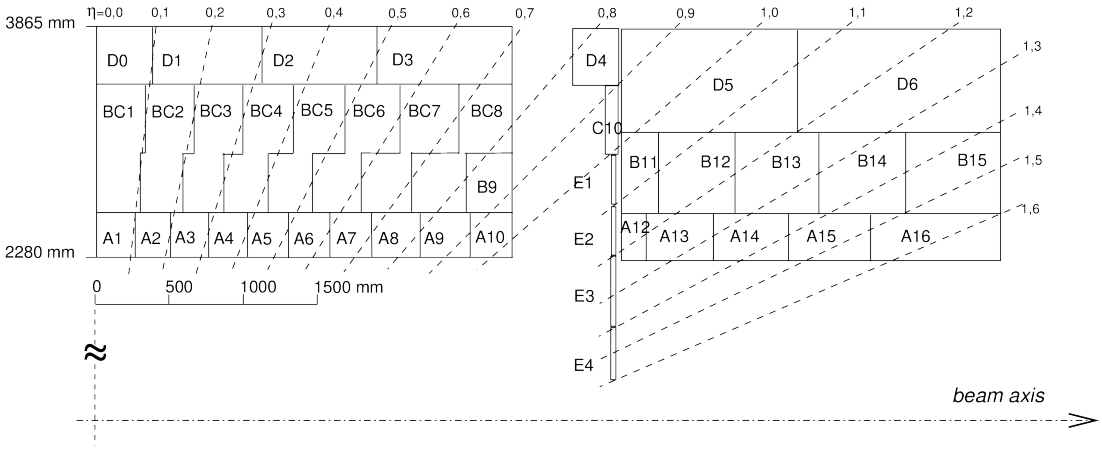

Figure 2.2: Mapping of individual cells in a module of TileCal for the central barrel (on the left side) and extended barrel (on the right side) [5].

plification ratio in high gain branch compared to the low gain branch is 64:1. This method allows for measurement of a very large scale of energies, from noise, up to around 800 GeV energy signal. The low gain branch also guarantees differentiation between the noise and muon signal. There is an ADC (analogue-to-digital) converter present in each branch reading and sampling the shaped pulse from PMTs. The signal is stored in ADCs for up to several μs and it is sent further towards the next trigger level if L1 Trigger System accept is approved.

L1 Trigger System approves or denies an event based on the synthesis of information from its components:

- L1 Calorimeter Trigger
- L1 Muon Trigger
- Central Trigger Processor

The event selection happens at 3 trigger levels. Trigger System reduces the number of events from approximately 4×10^7 to a maximum of 500 cases. It is necessary so that the storage system is able to handle all of the new events.

3. Test beam

The focus of this thesis is on TileCal test beam data. Test beams are performed in CERN SPS North Area with 3 chosen modules of Tile Calorimeter 2, the hadronic calorimeter at ATLAS experiment. Used particle beam comes from SPS (Super Proton Synchrotron), as explained in section 3.1.

3.1 SPS

Super Proton Synchrotron, or SPS, is one of the accelerators in the complex CERN accelerating system, as shown in figure 3.1. SPS, as a proton-antiproton collider, served in 1983 for the discovery of the W and Z bosons [9]. Currently, SPS is accelerating exclusively proton beams.

The protons coming to SPS are pre-accelerated in several consecutive steps [7]:

- up to 50 MeV in linear accelerator Linac2
- up to 1.4 GeV in circular accelerator Proton Synchrotron Booster
- up to 25 GeV in circular accelerator Proton Synchrotron

Afterwards, the protons are sent to the circular accelerator SPS, where they are accelerated up to 450 GeV. For the purposes of the ATLAS experiment, the SPS would send the proton beam to LHC for further acceleration. However, for the TileCal test beam area, H8 SPS beam is used directly. SPS also provides beams to NA61/SHINE, NA62 and COMPASS experiments.

After leaving SPS ring, the composition of the proton SPS beam can be adjusted. Before coming to the testing hall, H8 proton beam usually collides with a target made from Beryllium. The resulting secondary beam consists mainly of pions, then also from protons, muons and electrons. We will use this type of beam in chapter 5. Using a magnet system, we can then choose specific energy of the secondary beam.

This beam can be further adjusted to form a beam containing mainly muons. Muon beam is produced by colliding the secondary beam (consisting mainly of pions), with a large concrete block. Pions from the beam sent towards the concrete block are interacting with its matter producing hadronic showers or decaying to muons. As hadrons interact strongly with the matter of the concrete block, hadronic showers are almost fully absorbed in its volume. Therefore, the beam coming out of the concrete block will be mainly formed by the muons and neutrinos from pion decays. We will be interested in the muon beam in chapter 4.

3.2 Test setup

The setup of the TileCal test beam area is shown in figure 3.2, where the H8 particle beam comes from one side (left in the figure) of the testing area. The H8 beam then traverses 3 Cherenkov detectors (one of them is outside of the experimental area and therefore not displayed in figure 3.2), 2 scintillators, 2 beam chambers and then it finally hits the TileCal modules. There is also a muon hodoscope,

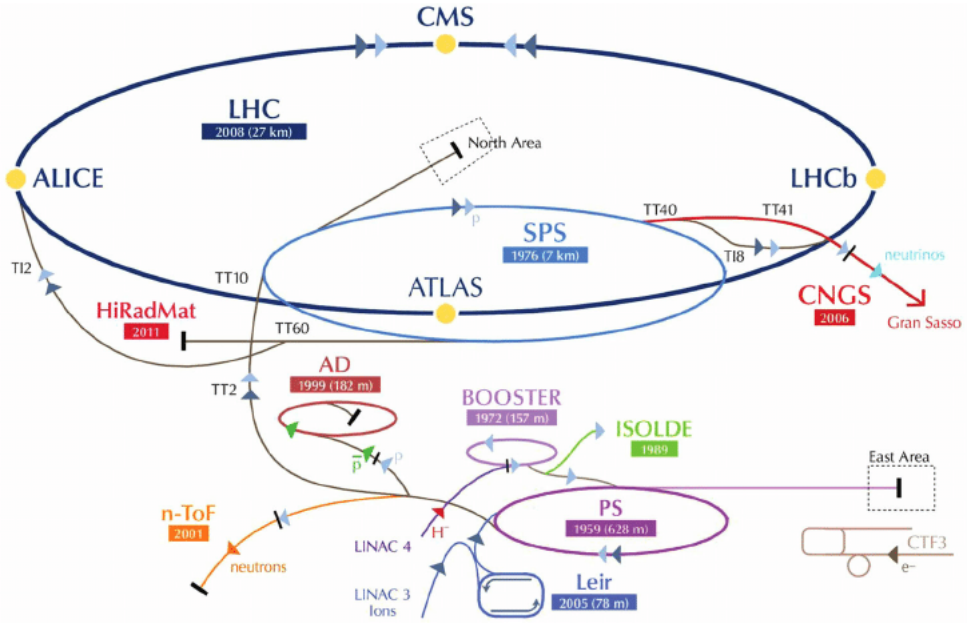

Figure 3.1: Complex accelerator system in CERN [7].

behind the TileCal modules, useful at a certain angle of incidence of the beam. Each of the detectors on the beamline has its own role in supporting the choice of right events during analysis. We are going to discuss it in chapter 4.1 and 5.1.

All of the TileCal test modules (see figure 3.3) are mounted to a robust scanning table, which allows for shifting and turning the modules to the desired position. Two bottom layers consist of central barrel modules M0 and LB65 (from the bottom up). The top layer is made up of one extended barrel module EBC65.

Setup in figure 3.2 is used for the experiments in the next chapters. We are using $\theta = -90\,^\circ$ position (see figure 3.3) of TileCal modules for the purpose of muon response analysis in chapter 4. For the pion leakage analysis in chapter 5, TileCal module is placed in projective geometry (same as in figure 3.2), but the exact angle of rotation is changing depending on which cell is targeted.

We introduce the pseudorapidity η for describing the angle of the beam with respect to the TileCal modules. It holds [11]

$$\eta = -ln\left(tg\frac{\theta}{2}\right), \tag{3.1}$$

where θ is a polar angle measured in the horizontal plane. Beam under an angle $\theta = 0\,^\circ$ is perpendicular to the front side of the TileCal modules (see figure 3.3).

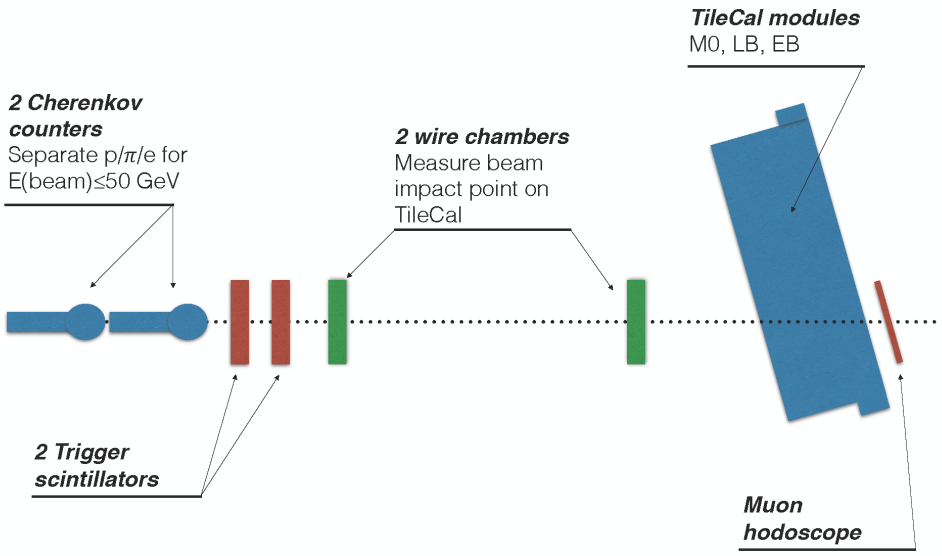

Figure 3.2: Setup of test beam equipment [8].

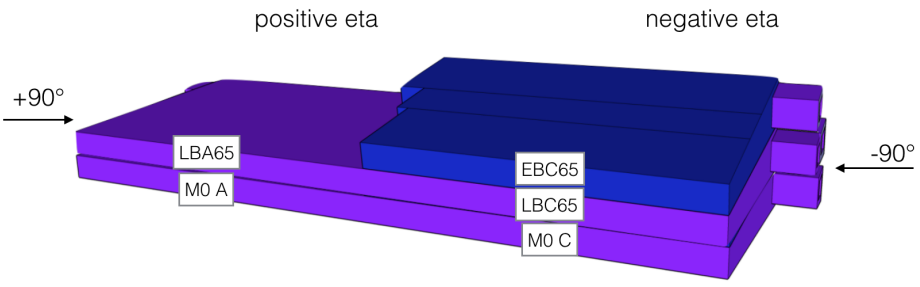

Figure 3.3: TileCal test modules from the front [8].

4. Muon response in non-projective geometry

The goal of muon response analysis is to compare the response in A, B and D cell rows in the extended calorimeter module EBC65 for calibration purposes. For this analysis, two sets of test beam data from November 2018 were used. For run number references see table 4.1, where the runs are listed according to the tile targeted by the beam during the run time. Both of the sets contain data from 300 GeV muon beams from SPS accelerator impinging on the TileCal modules in the same experimental setup, described in section 3.2. Each run consists approximately from 30 000 events (before cuts).

Table 4.1: List of runs for muon analysis.

Tile	**Set 1**	**Set 2**
1	811635	811848
2	811633	811846
3	811631	811844
4	811630	811842
5	811628	811841
6	811627	811839
7	811626	811838
8	811624	811836
9	811622	811835
10	811621	811833
11	811620	811832

As we are interested in comparing the muon response among cell rows, TileCal modules were turned to the angle $\theta = -90^\circ$ (see figure 3.3). From the beam perspective, we would see Tile 1 (part of cell row A) at the left end and Tile 11 (part of cell row D) at the right end of the TileCal extended module.

During the experiments, there was only one functional threshold Cherenkov detector (Cher2) and muon hodoscope was not used. Both scintillators, as well as, both beam chambers functioned correctly.

In the beginning, we reconstructed the PMT-to-cell mapping for EBC65, as the mapping available was not valid any more. Firstly, we checked which PMTs are attributed to the same cell via a study of the correlation between PMTs. Then, based on the energy response, we found a corresponding cell for each couple of associated PMTs. With the runs available it was possible to check the correctness of the mapping with several runs shooting to the different tile rows within the same cell row.

4.1 Choice of events

In this section, we explain the process of picking the muon particles with specific characteristics (described in the sections below) that we require for response

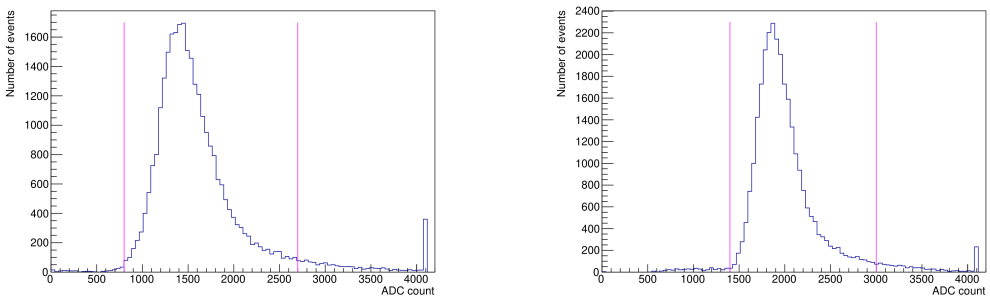

(a) Scintillator 1.

(b) Scintillator 2.

Figure 4.1: Signal in scintillators.

comparison among the A, B and D cell rows.

All of the cuts mentioned in the sections below were applied to all of the runs in table 4.1. It is possible to use the same cuts, as all of the data were gathered under the same conditions, with the 300 GeV SPS muon beam applied, in the detector position of $\theta = -90\,^{\circ}$ (see 3.3) and always targeting center of the relevant tile. Data for both run sets were collected just two days apart. Firstly, cuts were set for one run. Afterwards, the cut accuracy was tuned and checked for the rest of the runs in Set 1 and Set 2.

In the following subsections, we will use data from the run number 811848 (corresponding to the Tile 1 in Set 2) for a visual demonstration of the signal and the cuts applied. As the first detector on the beamline, the Cherenkov detector, was not used for cuts, we will begin by describing the cuts on scintillator signal.

Please note that X-axis refers to the horizontal direction and Y-axis refers to the vertical direction both when describing tiles and detectors on the beamline.

Scintillators

Scintillators serve for TileCal as triggers of the signal collection. They are emitting scintillation due to de-excitation of molecules/atoms excited previously by a charged particle traversing the matter of the scintillator. In our analysis, we applied cuts on the bottom of the scintillator spectrum to eliminate the noise. The cut at the top end of the scintillator spectrum removes events with high ionization, as this could mean more particles are ionizing at the same time (overlap).

The criteria for choosing events based on the scintillator signal resulted in accepting events with ADC count of:

- 800 - 2 700 in scintillator 1
- 1 400 - 3 000 in scintillator 2

For the signal visualization in both scintillators with highlighted cuts, see figure 4.1.

Beam chambers

- **Multi-hit**

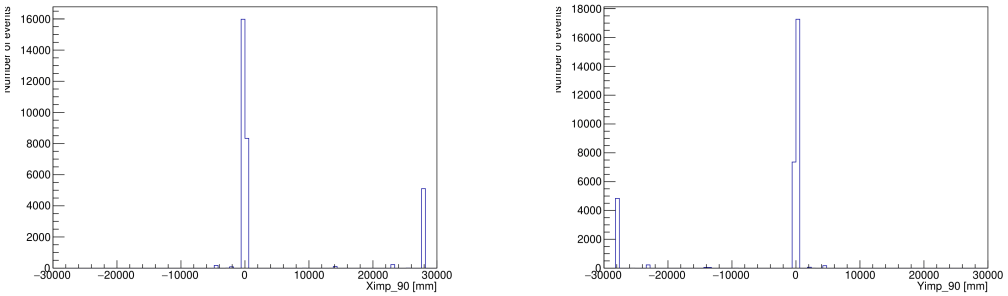

(a) X-axis. (b) Y-axis.

Figure 4.2: Impact point off-values for both axes.

For both X and Y beam chamber axes, we have two data points for each event. We get the value of the first and the last hit in the beam chamber. In our analysis, we set the value of the first and last hit equal. Equality allows us to choose only the single-hit events and avoid multi-hits, as these could lead to data misinterpretation.

- **Divergence**

  Beam chambers show information about transversal beam profile in the X and Y-axis. We have two beam chambers on the beamline gathering data and therefore we obtain two beam profiles (see figure 4.3 for reference). The difference of the beam profile in the first and second beam chamber shows divergent particles present in the beam.

  We took the difference of beam chamber profiles, fitted the difference iteratively with Gaussian distribution function and applied a cut at $+2\,\sigma$ and $-2\,\sigma$ from the mean of the distribution. This way, we considerably eliminated divergent particles from the muon beam. We applied this method separately in the X and Y-axis.

Impact point

Impact point variables (noted X_{imp90} and Y_{imp90} in this analysis) are calculated from beam chamber coordinates and give us an idea about what the beam looks like at the level of impingement on the TileCal module.

We applied cuts on the impingement variables X_{imp90} and Y_{imp90} for several reasons:

- **Off-values**

  There is a need to discard off-values appearing on the scale of meters (see figure 4.2), while none of the tiles is larger than 40 cm in X or Y direction.

- **Central beam**

  Next important consideration is the mechanical structure of the TileCal detector. In each tile row, there are two special structures inside. One of them is a rod serving as mechanical support for the detector. The other

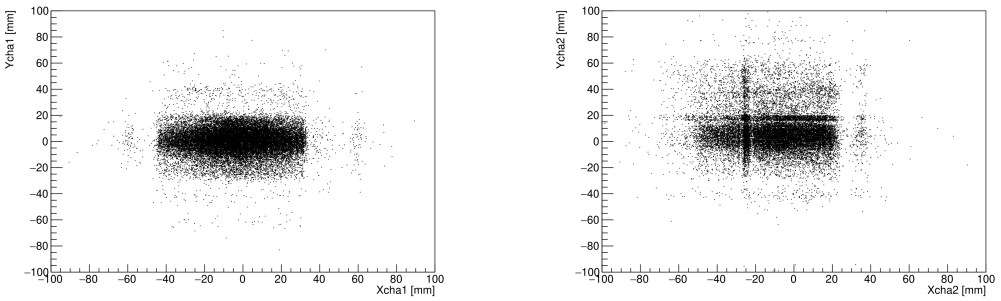

(a) Beam chamber 1.

(b) Beam chamber 2.

Figure 4.3: Beam profile as recorded by beam chambers.

is a pipe for administrating radioactive Caesium into the detector during Caesium calibration.

Both structures influence data readout. According to our investigation, the mechanical structures are causing the presence of low energy events in total energy histogram. As the pipe and the rod are located at approximately + 3.5 cm and - 3.5 cm in the horizontal (or X-axis) direction from the centre of the tile, we cut the particles coming to this area and effectively chose the beam symmetric around 0.

We also chose central particles in a vertical direction through applying a similar cut in the Y-axis. It is useful also because the tile response is not uniform throughout the tile (see section 4.3).

We perform the central cut at the level of impact point rather than at the beam chamber because there is still a small effect of divergence present even after applying the cut for divergent particles. Thus, it is better to perform the cut as close to the TileCal module as possible.

- **Beam chamber issue**

  When we look at the beam profile at the beam chamber 1 and 2 (shown in figure 4.3), we observe an issue (cross shape in the beam profile) in the second beam chamber. While this is a technological issue of the beam chamber, it affects the beam itself and the changes are pronounced also at the impact point level (see figure 4.4).

  This results in a secondary peak of events at ≈ -25 mm in the X direction at the level of impingement, as seen in figure 4.5(a). We set the cuts so that we avoid this area.

  Because of the same reason, we observe a secondary peak of particles also in the Y direction at ≈ +20 mm. We do not cut this area, as this cut lowers down the number of events by more than 1 000 without providing a major improvement in results.

To summarize this section, for the reasons described above, we performed event rejection at the level of the impact point. The cuts were set at ± 24 mm in the X-axis and ± 30 mm in the Y-axis direction. The cuts applied to the impact

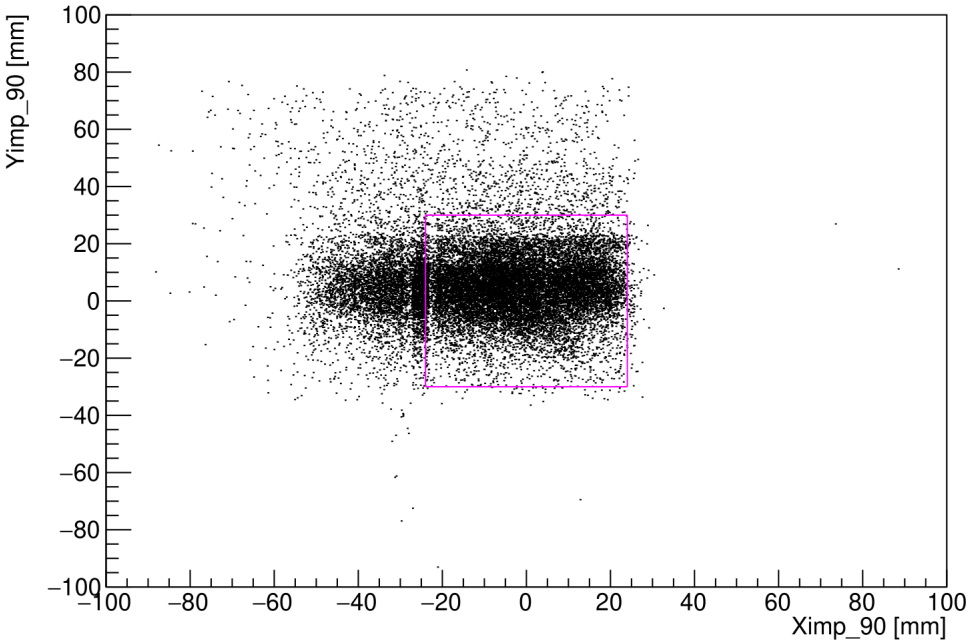

Figure 4.4: Beam profile at the impact point level.

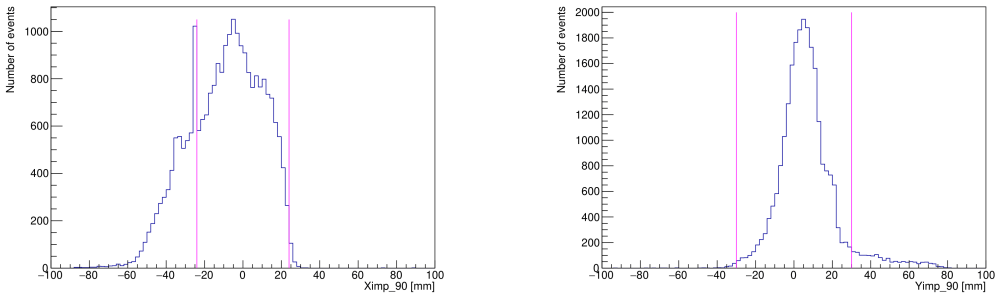

(a) X-axis. (b) Y-axis.

Figure 4.5: Impact point values and corresponding cuts.

point variables in the X and Y direction are displayed in figure 4.5(a) for X-axis, 4.5(b) for Y-axis and in figure 4.4 for the whole beam profile.

The energy in the first and the last cell

Muons at the energy of 300 GeV are losing energy in calorimeters almost exclusively through the process of ionization. That is why they always traverse through the whole calorimeter depth. To make sure, we were working with muons, we set a requirement that the signal from one specific event is present in the first, as well as, in the last cell of the specific tile row we are aiming at.

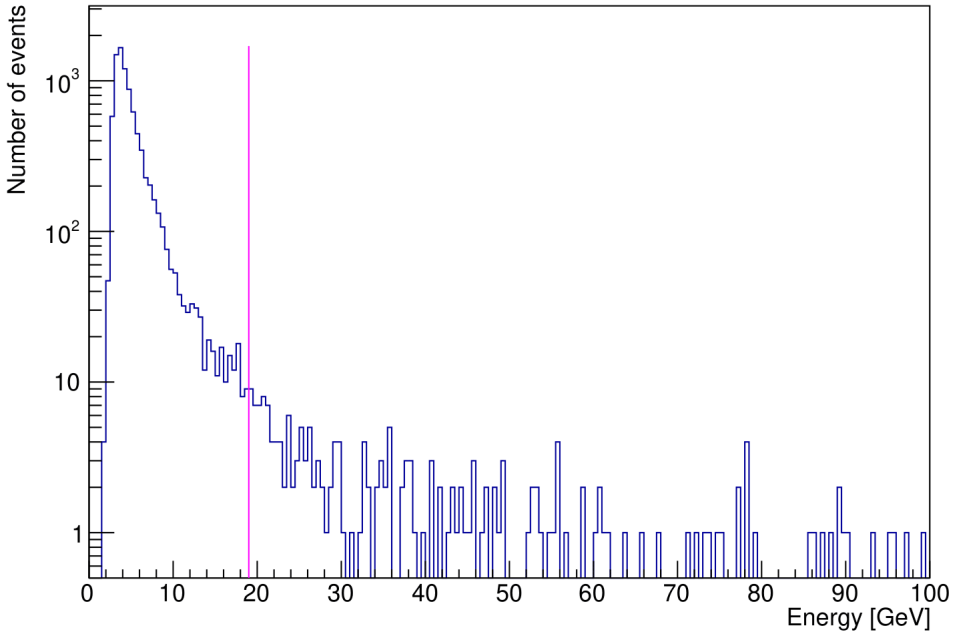

Figure 4.6: Truncated mean cut of the energy spectrum.

Truncated mean

As we have some events at larger energies comparing with the main part of the distribution, the truncated mean is a better estimator for the energy deposited in the calorimeter than the mean value. Therefore, we carried out truncated mean, cutting the top $2,5\,\%$ of events in terms of the total energy (see figure 4.6) to eliminate the influence of the energy data points at the tail of the distribution. Then, we took the mean of the remaining $97{,}5\,\%$ of entries. This method was previously used in the article [10]. Truncated mean values were then used for the calculation of B/A and D/A ratios.

4.2 Radial electromagnetic calibration

Coming back to the purpose of studying muon response, in this chapter we are interested in the electromagnetic calibration (see chapter 2.2). In the beginning, the electronics is calibrated to obtain the conversion constant from ADC to pC value. The next step in the calibration, radial electromagnetic calibration, consists of two calibration stages.

Firstly, the calibration constant for the pC to GeV conversion is determined in projective geometry. For this purpose, the electron beam is radiating TileCal module under $20\,^\circ$ angle (same as in figure 3.2). However, electrons lose approximately $90\,\%$ of their energy in A cells. Therefore, the calibration constant is relevant primarily for A cell row.

Secondly, we need to consider the differences between cell rows. Calibration via radioactive source is done via the pipe at the external radius of each tile row. Since each tile row has a different tile size, the distance from the Caesium pipe to

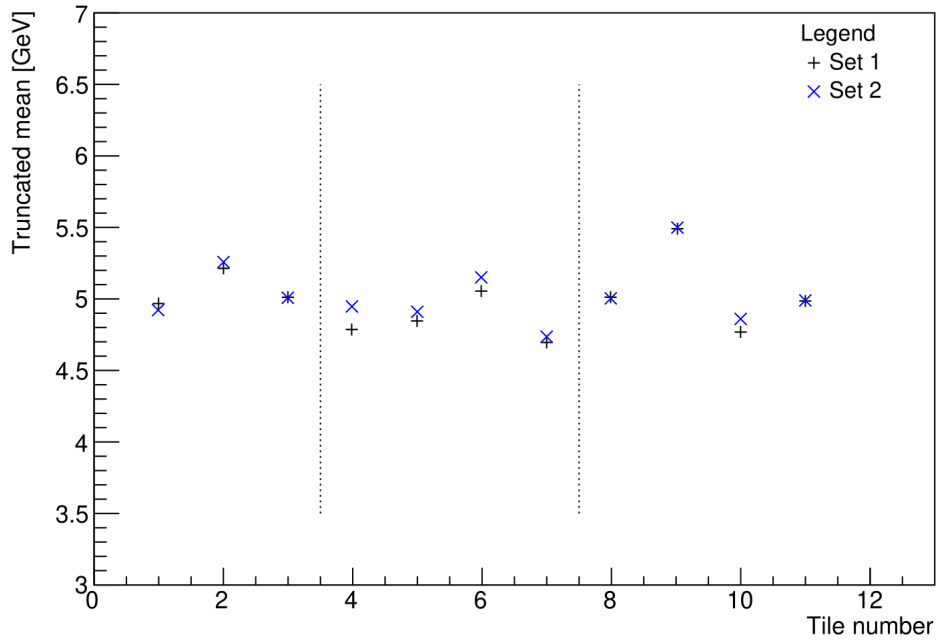

Figure 4.7: Truncated mean energy results for both sets.

the middle of the tile varies for each tile row. Therefore, Caesium is calibrating the middle of the tile row differently for each tile row. This means, for example, that for larger tiles (tile row 11 being the largest) Caesium calibration causes muon response to be lower in comparison to other tile rows. Thus, the response of B and D cell rows is lower compared to cell row A. Therefore, B/A and D/A ratios should be smaller than 1 and correction factors need to be determined to adjust for cell row response levels. Correction factors for B and D cell rows were previously established in a study of production modules for TileCal [10].

4.3 Results

We performed a review of electromagnetic correction factors for cell rows for the EBC65 extended barrel module of TileCal, presented in the article [10].

After applying the cuts to choose the right muon events, we measured truncated mean energy response for each tile row (see figure 4.7). Two vertical lines in figure 4.7 divide the 11 tile rows into 3 cell rows. There are:

- 3 tile rows in A cell row
- 4 tile rows in B cell row
- 4 tile rows in D cell row

Based on the truncated means for all the tile rows (see figure 4.7), we computed an average truncated mean energy response for each cell row, as seen in formula 4.1.

$$trunc_A = \frac{trunc_{Tile1} + trunc_{Tile2} + trunc_{Tile3}}{n_A} \tag{4.1}$$

where n_A is the number of tile rows in the A cell row and $trunc_i$ refers to the truncated mean of the tile or cell designated as i.

Then, we computed the cell row response factors B/A and D/A, from the average truncated means per cell row. B/A is the response factor for B cell row of the extended barrel with respect to the A cell row and D/A analogously for D cell row. Response in A cells is set to one to have a reference point, as the A cell row response has already been calibrated beforehand with electrons in projective geometry setup (described section 4.2). Resulting response ratios from our analysis are displayed in table 4.2 for runs in Set 1 and table 4.3 for Set 2 run data.

Table 4.2: Response ratios for Set 1.

	Ratio
B/A	0.957 ± 0.004
D/A	1.001 ± 0.003

Table 4.3: Response ratios for Set 2.

	Ratio
B/A	0.975 ± 0.006
D/A	1.005 ± 0.006

In our test beam data, the correction constants for B/A and D/A, established in [10], were already applied. Consequently, it is expected to obtain results equal to one for all the ratios.

For D/A ratio the result is perfectly aligned with the expectations and is equal to one when taking the error range into account. This is true for both data sets. The situation is a little different for B/A ratios. B/A ratio differs from the desired result by $\approx 4\,\%$ for Set 1 and by $\approx 2\,\%$ for Set 2.

While the deviation in the B/A ratios is not radical, we can look at the possible causes behind it. Firstly, the middle of the tile in the test beam experiments is set with an insufficient accuracy of 20 mm. Secondly, the tiles themselves do not give a uniform response over their whole surface. Both of these issues can bring additional error into the results and we discuss them in detail in the following sections. Finally, EBC65 module used in the analysed test beam runs is different to the modules used directly in the ATLAS experiment. Therefore, we can observe a certain incoherence when comparing the results to the article [10]. It is difficult to quantify the difference as this specific module type, labelled IFA65, was not used in the analysis [10].

Tile center

One of the typical test beam issues is the alignment and there arises the question of how accurately is the beam directed to the tile center. The table carrying modules can be moved with limited precision. At the beginning of the test beam in November 2018, there was a great effort put on aligning the module, as accurately as possible. Nevertheless, we can talk about the tile center only with the accuracy

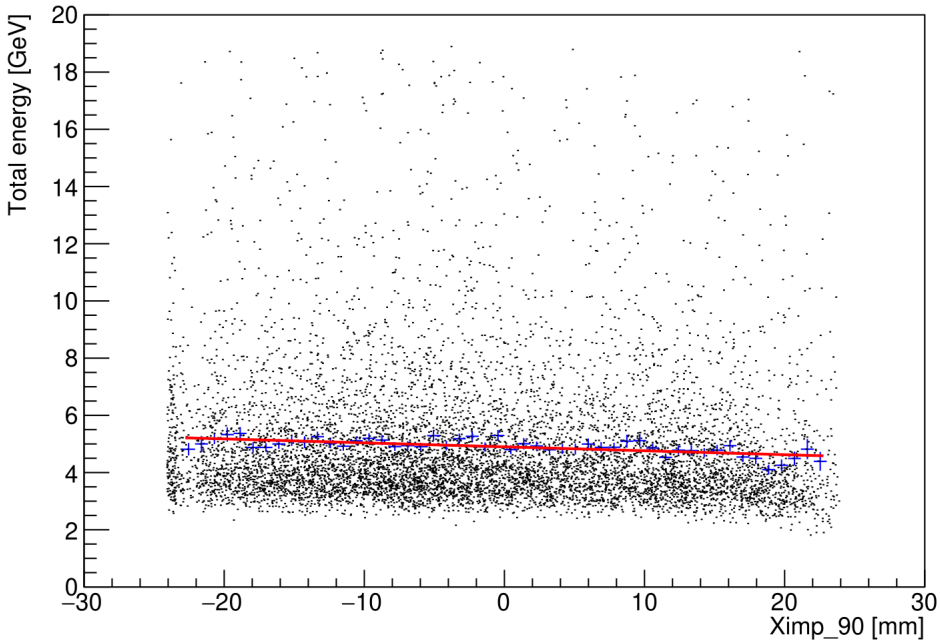

Figure 4.8: Total energy dependency on impact point in the X direction for Tile 1, Set2.

of up to 20 mm. Also, the center of impact point histogram (see figure 4.5(a)) does not have to be the physical center of the tile, as the impact point is calculated from beam chamber coordinates.

Tile uniformity

We performed a check of the total energy dependency on the impact point in the horizontal direction. Ideally, energy response should be independent of the impact point and therefore have a uniform response throughout the surface of the tile. However, in figure 4.8 we see a linear dependency on the impact point.

We symmetrized the beam with respect to the impact point variable to investigate the influence it has on the ratios B/A and D/A. At first, we performed symmetrization of the event distribution dependency on impact point. The symmetrization was based on Gaussian distribution. Afterwards, we retrieved the symmetrization weights for individual events. In the end, we applied these weights to the energy distribution event-by-event.

We symmetrized the beam profile once according to the Gauss distribution centered in zero and then moving the center to the mean of event distribution obtained without symmetrization ≈ -9.5 mm. This approach resulted in a new set of B/A and D/A ratios, as shown in tables 4.4 and 4.5.

Symmetrization of the beam leads to slightly different coefficients but does not make the result better for B/A coefficient. The outcome is consistent with the linear dependency of total energy on the impact point (see figure 4.8). The dependency

$$E_{tot}\,[\mathrm{GeV}] = k\,X_{imp90}\,[\mathrm{mm}] + q, \tag{4.2}$$

where $k = -0.0138\,[\mathrm{GeV/mm}]$ and $q = 4.8997\,[\mathrm{GeV}]$ implies that the difference between the second and third column in ratio tables 4.4 and 4.5 should be $\approx 2\,\%$. The contribution of the tile not being uniform throughout its surface to the systematic uncertainty is by one order larger comparing with the previously established uncertainty in tables 4.2 and 4.3.

Table 4.4: Ratios B/A and D/A after Gauss symmetrization for Set 1.

	No sym.	**Sym. in 0**	**Sym. in mean**
B/A	0.957	0.960	0.936
D/A	1.001	0.986	0.976

Table 4.5: Ratios B/A and D/A after Gauss symmetrization for Set 2.

	No sym.	**Sym. in 0**	**Sym. in mean**
B/A	0.975	0.963	0.957
D/A	1.005	1.000	0.994

5. Pion response in projective geometry

In this chapter, we study pion response in the projective geometry to determine the dependency of the energy leakage from TileCal based on the angle of incidence of the pion beam. For this purpose, we used again data from test beam of November 2018, where H8 SPS 290 GeV pion beam was impinging on TileCal module LBC65.

All the runs used for the analysis are listed in table 5.1. The runs are ordered based on the cell number that was being targeted by the pion beam. For reference about the positioning of the specific cells see figure 2.2. Depending on which cell is targeted during the run, the scanning table is changing angle with respect to the beamline. Therefore the η (see equation (3.1)) varied from -0.05 for A-1 cell to -0.65 for A-7 cell.

Each runs consists approximately of 100 000 events.

Table 5.1: List of runs for pion analysis ordered according to the respective cell number.

A-1	**A-2**	**A-3**	**A-4**	**A-5**	**A-6**	**A-7**
811476	811481	811490	811498	811512	811525	811537
811478	811483	811491	811499	811513	811526	811538
811479	811484	811493	811501	811514	811527	811539
	811485	811494	811503	811515	811529	811540
	811487	811496	811505	811517	811530	811541
	811488		811506	811519	811531	811543
			811507	811521	811532	811544
			811509	811522	811534	811545
			811510	811523	811535	811546
			811511	811524	811536	811547

5.1 Event choice

Similarly to chapter 4.1, we started by applying cuts to choose the particles with desirable properties. In this section, we will comment on the cuts for signal observed in scintillators and beam chambers. In the next section 5.2, we will break down the identification of particles present in the beam (muons, electrons, protons and pions).

Cherenkov detector was not used for event choice, as it did not provide us with additional information. We aligned the used cuts with the cuts employed in a previous pion analysis of test beam data from November 2018 [12].

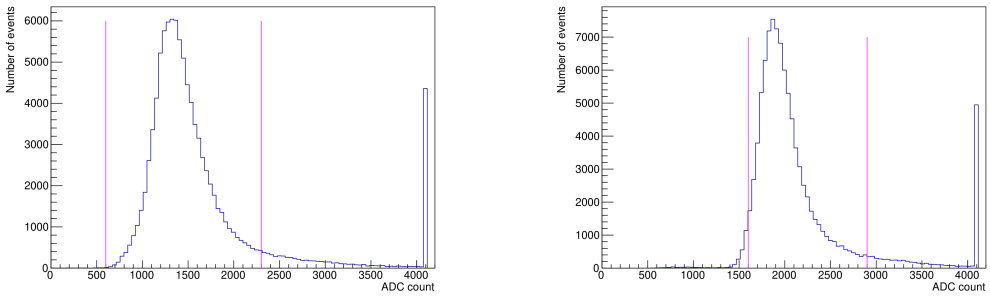

(a) Scintillator 1.

(b) Scintillator 2.

Figure 5.1: Scintillator signal for hadron beam (run 811503).

Scintillators

As explained in chapter 4.1, we applied the cuts on the lower and upper end of the scintillator spectrum. We demanded the ADC count to be:

- 600 - 2 300 in scintillator 1
- 1 600 - 2 900 in scintillator 2

For a visual representation of the cut on scintillators see figure 5.1.

Multi-hits and divergence

In the same way as in the previous chapter concerned in the muon analysis, we performed cuts to avoid multi-hits and divergent particles. We put into use the same principles, as laid out in chapter 4. To summarize, firstly, we rejected multi-hits by requiring that the first and the last recorded hit in the beam chamber is the same event. Secondly, we avoided divergent particles by choosing the range of particles from $-2\,\sigma$ to $+2\,\sigma$ around the mean of the difference of the two beam chamber profiles. We selected events in this way both in X and Y beam chamber axes.

Central beam

We chose the central part of the beam by applying the cut at ± 40 mm in the X beam chamber axis and at ± 30 mm in the Y-axis. The cuts are displayed in figure 5.2.

5.2 Particle identification

Hadron SPS H8 beam contains a mixture of different particles. We were interested in hadrons, mainly in pions. For that purpose, we tried to identify and cut muons and electrons off the beam. Afterwards, we moved on to the distinction between protons and pions. We will describe the identification of each particle type in the following sections.

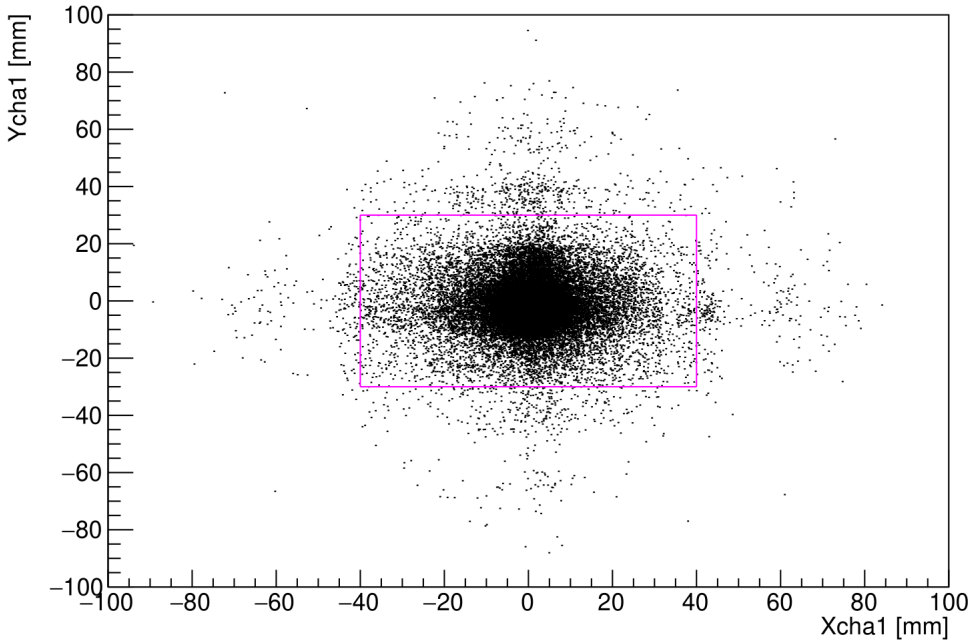

Figure 5.2: Beam chamber 1 signal with applied cuts (run 811503).

Muon veto

To decline muon events we used the total energy response measured in the TileCal test modules M0C, LBC65, EBC65. We applied a cut at $3\,\sigma$ below the mean value of energy and rejected events with lower energy (see figure 5.3). According to the article [13], this cut eliminates the vast majority of muon events in the beam, while not decreasing the number of pion events present.

Electron identification

It is supposed that in the SPS hadron beam of the energy 290 GeV there should not be electrons in the beam. Nevertheless, we verified this hypothesis in two ways:

- **C_{long} and C_{tot} functions**

  Electrons and hadrons initiate different types of showers in the detector. Electrons produce purely electromagnetic showers which are geometrically narrow and $\approx 90\,\%$ of the shower is absorbed in the A cell layer of the TileCal detector. Hadrons, on the other hand, trigger mainly hadronic showers with electromagnetic components. Hadronic showers are geometrically much wider than purely electromagnetic showers and they are also longer - the products of hadronic showers can be measured in all the layers of TileCal, including D cell layer.

  These differences in the shower properties can be utilized to distinguish electrons from hadrons by using C_{long} and C_{tot} functions [15].

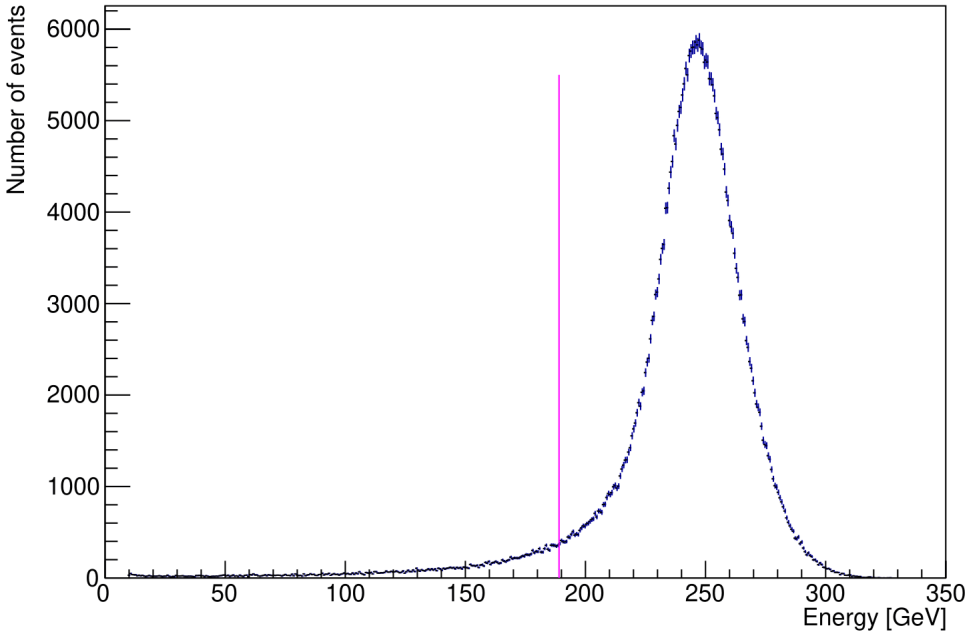

Figure 5.3: Muon cut on the energy spectrum (all A-4 cell runs listed in table 5.1).

C_{long} function is defined as

$$C_{long} = \sum_{i} \sum_{j=1}^{2} \frac{E_{ij}}{E_{beam}}, \tag{5.1}$$

where the index i runs over the cells in the 3x3 tower around the point of impingement and the index j runs over the radial cell layers. E_{ij} stands for energy in one cell and E_{beam} refers to the hadron beam energy 290 GeV.

C_{tot} function is defined as

$$C_{tot} = \frac{1}{\sum_c E_c^\alpha} \sqrt{\sum_c \frac{(E_c^\alpha - \sum_c E_c^\alpha / N_{cell})^2}{N_{cell}}}, \tag{5.2}$$

where the index c runs over all the cells in the 3x3 tower around the point of impingement, N_{cell} refers to the number of the cells in the tower taken into account, E_c represents energy in one cell and exponent α was tuned in simulations published in [15] to the value of 0.6. This α value assures the best possible differentiation between electrons and hadrons.

As seen from equations (5.1) and (5.2), it is very important to consider the mapping of the TileCal modules when computing C_{long} and C_{tot} values. We checked the mapping for the right half of the modules (see figure 3.3). We examined M0C and LBC65 central barrel mapping [14] observing the correlation of signal from both PMTs in one cell. In the LBC65 we did not use PMT number 24 (from the cell A-6) and 26 (from the cell D-2). The missing signal was substituted by taking the signal from the second PMT connected to the same cell, PMT number 25 in cell A-6 and number 27

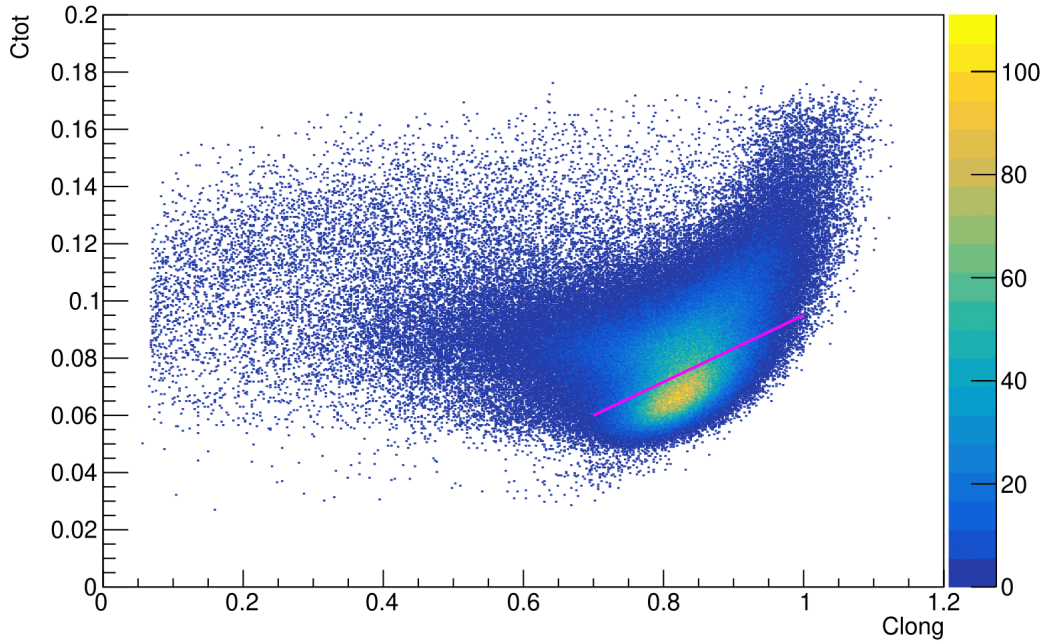

Figure 5.4: C_{tot} versus C_{long} functions. Both formulas are stated in the equations (5.2) and (5.1) (all A-4 cell runs listed in table 5.1).

in cell D-2, twice. For the extended barrel module EBC65 the reconstructed mapping from chapter 4 was used.

We show calculated C_{long} and C_{tot} functions in a 2D histogram 5.4. We observe two areas in the histogram, as suggested by the pink line diving them. We refer to the peak below the pink line as the primary peak and to the other one as the secondary. We investigated both regions further by studying the energy response in cell rows, longitudinal profile and overall energy response for each of the regions with the aim of understanding the distinction between them. We depicted the overall energy response for both areas in figure 5.5. The mean value for the primary peak (blue line in the figure) is $247.1 \pm 11.78\,\text{GeV}$ and for the secondary peak (red line in the figure) the mean is $246.3 \pm 18.38\,\text{GeV}$. Practically the same value of the mean energy for both regions indicates the particles from the primary area are not different from the secondary area particles.

The properties of electromagnetic showers above also suggest that electrons should have higher C_{long} value than hadrons. Evidently, we do not recognize such a peak in figure 5.4, which indicates the absence of electrons in the beam.

Finally, we concluded that the two areas in figure 5.4 do not represent two different types of particles, but merely electromagnetic and hadronic components of a hadron induced shower. Primary peak (blue line in figure 5.5) corresponds to the electromagnetic shower component. Hadronic component is represented by the secondary peak (red line in figure 5.5).

- **Energy dependency on the impact point**

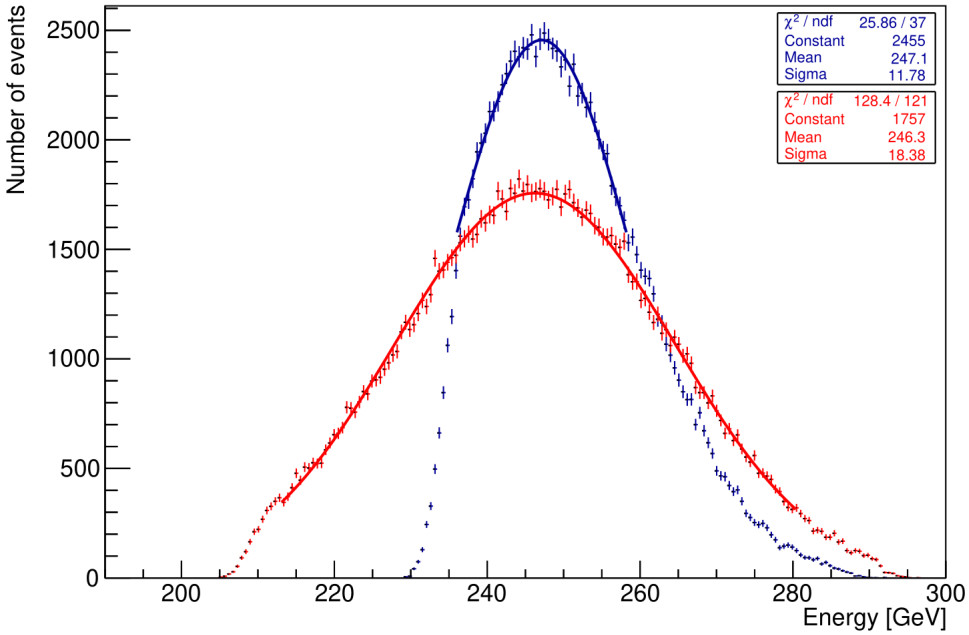

Figure 5.5: Energy response for both peaks in histogram 5.4 (all A-4 cell runs listed in the table 5.1).

Another indicator of electron presence in the beam would be a sine shape of energy dependency on the impact point variable X_{imp}. The oscillation pattern appears due to the combination of the mechanical structure of the Tile Calorimeter and the narrow character of the electromagnetic showers. We can describe the dependency on impact point as [10]

$$E_{tot}(X_{imp}) = p_0 \left[1 + p_1 \sin\left(\frac{2\,\pi\,X_{imp}}{p_2} + p_3\right)\right], \tag{5.3}$$

where parameter p_0 denotes the mean energy, p_1 refers to the relative amplitude of the oscillation, p_2 stands for the oscillation period and p_3 is a phase.

Considering we are investigating the dependency in A-4 cell (beam impinging under $\theta = 20\,^\circ$), it holds for the oscillation period

$$p\,[\mathrm{mm}] = 18\,[\mathrm{mm}]\cos(20\,^\circ), \tag{5.4}$$

where 18 [mm] refers to the distance from one scintillation tile to the other inside the structure of TileCal.

Nevertheless, we do not observe sine dependency from equation (5.3) in figure 5.6. This fact points out again the absence of the electrons.

As a result of studying C_{tot} versus C_{long} dependency, as well as, total energy dependency on the impact point in the A cell row, we can conclude there are no electrons present in the beam.

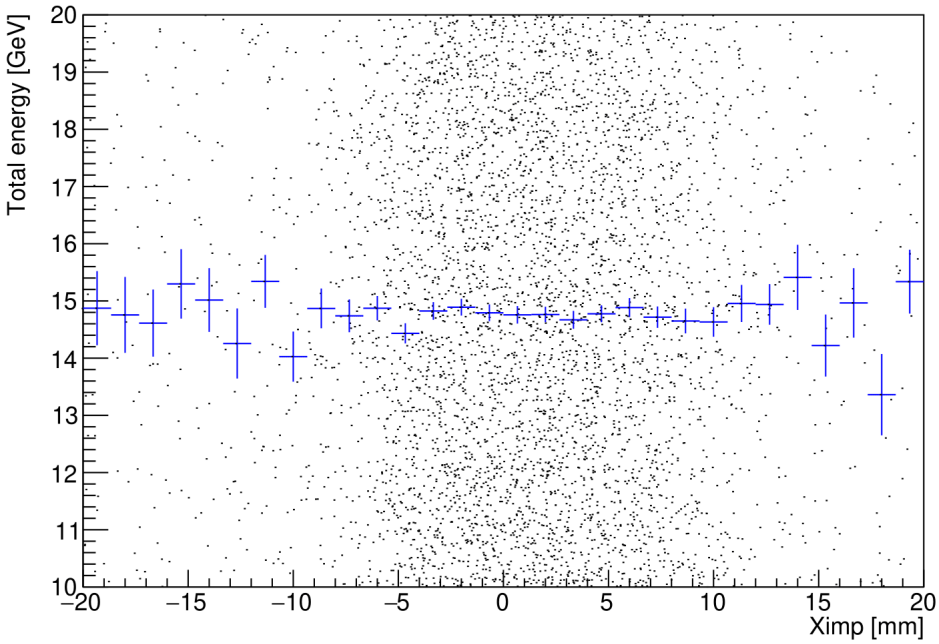

Figure 5.6: Energy dependency on impact point for A-4 cell (run 811503).

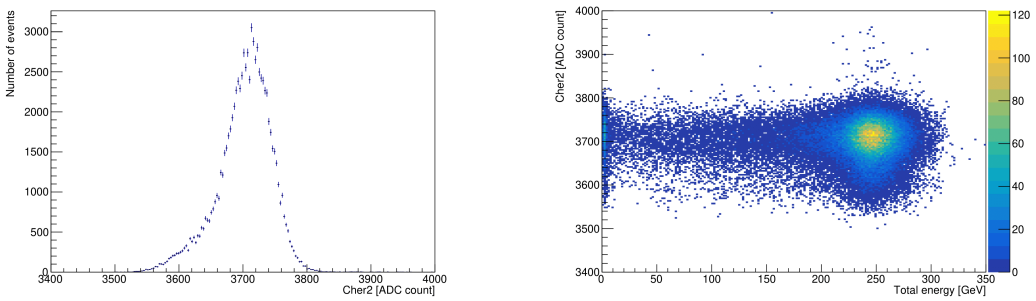

(a) Cher2 signal.

(b) Cher2 dependency on total energy.

Figure 5.7: Signal from the Cherenkov detector Cher2 (run 811503).

Protons and pions

To differentiate pions from protons we usually use Cherenkov signal. When the data for this analysis was being recorded, two out of three Cherenkov detectors on the beamline did not function properly. Thus, we were able to use only the signal registered in the Cherenkov detector Cher2. Note that in the following we will always refer specifically to the Cher2 detector when mentioning Cherenkov detector.

In accordance with the analysis in [10], we show the Cherenkov signal histogram in figure 5.7(a). Similarly, motivated by article [15] we display Cherenkov signal dependency on the total measured energy in figure 5.7(b). Nevertheless, in both histograms, we can only see one peak in the Cherenkov detector signal and therefore this approach does not result in hadron separation.

As Cherenkov signal does not resolve the issue of proton and pion separation,

we proceed with the analysis using the mix of proton and pion events. We continue to theoretical calculations and compare the data with theoretical results for both pure pion and pure proton beam.

5.3 Profile calculation

We aim to showcase the mean values of the energy recorded in the TileCal through η values from - 0.05 to - 0.75. We also choose to compare the experimental mean energy values to the theoretically established ones. To achieve that, we need to compute the theoretical longitudinal profiles for pure pion and pure proton beams at first. Afterwards, we will determine the mean energy for both theoretical profiles and experimental data.

To calculate the longitudinal profiles we use the analytical description [13]

$$\frac{dE}{dz} = N\left[\frac{wX_0}{a}\left(\frac{z}{X_0}\right)^a e^{-bz/X_0}\,{}_1F_1\left(1, 1+a, \left(b-\frac{X_0}{\lambda}\right)\frac{z}{X_0}\right)\right.$$

$$\left. +\frac{(1-w)\lambda}{a}\left(\frac{z}{\lambda}\right)^a e^{-dz/\lambda}\,{}_1F_1\left(1, 1+a, (d-1)\frac{z}{\lambda}\right)\right], \tag{5.5}$$

where N is a normalization constant, X_0 refers to the radiation length, λ stands for the nuclear interaction length and a, b, d, w are parameters. Their values depend on whether we calculate pion or proton longitudinal shower profile. Function ${}_1F_1(a, b, c)$ is the confluent hypergeometric function and the variable z represents detector depth in the direction of the beam impinging on the calorimeter.

Normalization constant, obtained by requiring

$$\int_0^\infty \frac{dE}{dz}dz = E_{\text{beam}} \tag{5.6}$$

where E_{beam} stands for the beam energy, is

$$N = \frac{E_{\text{beam}}}{\lambda\Gamma(a)\left(wX_0b^{-a} + (1-w)\lambda d^{-a}\right)}, \tag{5.7}$$

where $\Gamma(a)$ denotes the Gamma function.

To calculate the value of the radiation length X_0 we used formula for a compound material**??**

$$\frac{1}{X_0} = \sum \frac{w_j}{X_j}$$

where w_j and X_j are the weight and the radiation length for the jth element of the compound. We used an analogical formula also for the calculation of the interaction length λ. Using the formula above, we get values

$$X_0 = 2.24\,\text{cm}$$

$$\lambda = 20.55\,\text{cm}. \tag{5.8}$$

Adopting the parameters a, w, b and d from the article [13], we have

$$a_{\text{pion}} = -0.208 + 0.559\ln(E_{tot}[\text{GeV}])$$

$$w_{\text{pion}} = 0.647 - 0.0618\ln(E_{tot}[\text{GeV}])$$

$$b_{\text{pion}} = 0.243, \quad d_{\text{pion}} = 0.743 \tag{5.9}$$

for pions and

$$a_{\text{proton}} = 0.880 + 0.302\ln(E_{tot}[\text{GeV}])$$

$$w_{\text{proton}} = 0.676 - 0.657\ln(E_{tot}[\text{GeV}])$$

$$b_{\text{proton}} = 0.266, \quad d_{\text{proton}} = 0.784 \tag{5.10}$$

for protons, where E_{tot} is the mean energy left in the TileCal while considering no leakage outside the calorimeter. We establish the theoretical value of E_{tot} based on the beam energy E_{beam} and the knowledge of E_π/E_{beam} ratio from [10].

For verification of the correctness of formula (5.5), we calculated the longitudinal profiles (for pions and protons) at first for the maximal energy used in article [13], which is 180 GeV. For the beam energy $E_{\text{beam}} = 180\,\text{GeV}$, we have $E_\pi/E_{\text{beam}} = 0.866$ [10]. Thus, we use the total energy value $E_{tot} = 155.9\,\text{GeV}$.

The profile calculation, utilizing the mentioned constants and parameters, leads to the profile depicted in figure 5.8(a). After thorough verification of the profile values, we found that the pion longitudinal profile (blue line in the figure) is correct and matches the values in the article [13] (Table 4, page 176). However, the proton profile (red line in the figure) is obviously out of the expected range of values.

To correct the proton profile, we fitted retrospectively the parameter values a_{proton}, w_{proton}, b_{proton} and d_{proton}. The fitted parameter values for b_{proton} and d_{proton} are consistent with the expectations (see values (5.10)). Contrarily, we identified an issue with a_{proton} and w_{proton} parameters. To correct for this issue, we propose a new w_{proton} parametrization

$$w_{\text{proton}} = 0.676 - 0.0657\ln(E_{tot}[\text{GeV}]). \tag{5.11}$$

When recalculating the proton profile with this new parameter value, we obtain the result displayed in figure 5.8(b). After reviewing the function values and comparing to Table 5, page 176 in [13], we can confirm the correctness of the proposed w_{proton} value. In the following, we will work with the new w_{proton} parameter (5.11).

Note that for the comparison of the specific profile values for different z there is need to normalize the profile as required in [13].

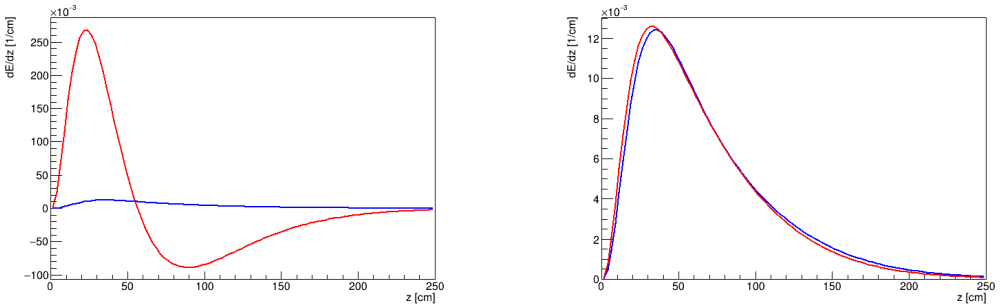

(a) Original w parametrization from [13].

(b) New w parametrization.

Figure 5.8: Theoretical longitudinal profile for 180 GeV hadron beams with different w parametrization. The profile is normalized in a way where $E_{\text{beam}} = 1$ in equations (5.6) and therefore in (5.7), as well. The blue line corresponds to the pion profile and the red line corresponds to the proton profile.

5.4 Mean energy

To obtain the theoretical mean energy value for different η, we integrated equation (5.5) from the beginning till the end of the calorimeter. The specific values of the calorimeter thickness vary depending on the angle of the beam. We listed the effective depths of the TileCal modules for different η in table 5.2. The constants used for the calculation of the longitudinal profile (5.5) and its integration are $E_{\text{beam}} = 290\,\text{GeV}$ and $E_{tot} = 155.9\,\text{GeV}$. The latter follows from the E_{beam} value and $E_\pi/E_{\text{beam}} \approx 0.9$ from article [10]. As for the radiation and interaction lengths X_0 and λ we use the values stated in (5.8).

Table 5.2: Effective depths of the calorimeter in centimeters for different η listed by the corresponding cell.

A-1	**A-2**	**A-3**	**A-4**	**A-5**	**A-6**	**A-7**
135.7	137.0	139.7	143.9	149.5	156.5	165.1

As a result of the profile integration, we obtain mean energy values for a pure pion beam and a pure proton beam. Both of the value sets are displayed in figure 5.9, where the pion results are represented by the blue triangles and the proton results by the red triangles.

The experimental mean energy values for each beam direction were retrieved from the total energy measured in the TileCal detector. We applied the cuts as detailed in the first two sections of this chapter, collected the energy values into an energy distribution histogram and took the mean energy value for each η. The experimental mean values are represented in figure 5.9 by the black cross markers.

In figure 5.9, we observe that the difference in the absolute value of the mean energy between experimental data and calculated values. The mismatch in the absolute value can be caused for example by an imprecise extrapolation of the E_π/E_{beam} ratio.

Nevertheless, we proceeded in our analysis to the comparison of the rising

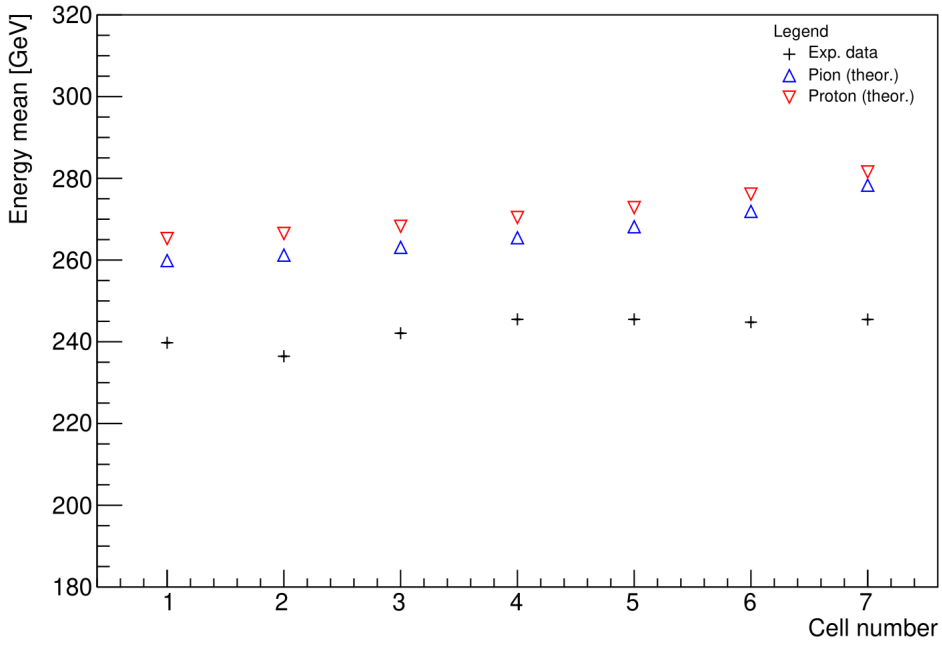

Figure 5.9: Mean energy dependency on the targeted cell.

tendency of the mean energy. We normalized the mean energy values to the mean response in the A-1 cell for each set of data independently. The result in figure 5.10 are showing the same gradual increase in values for the proton and the pion induced showers. The rising tendency of the theoretical mean energy values with the rising η is reproduced in the experimental values. However, we notice a difference for A-2 cell, which can be caused by a fault in the cell or in a PMT measuring energy for this specific η. For better explanation, we would need to study the response for a couple of different modules. When considering the beam impinging to the cell A-6 and A-7, we would expect the experimental values to rise more. Especially for A-7 cell, a slight decrease can be explained by the lateral energy leakage as we are close to a side of the TileCal module.

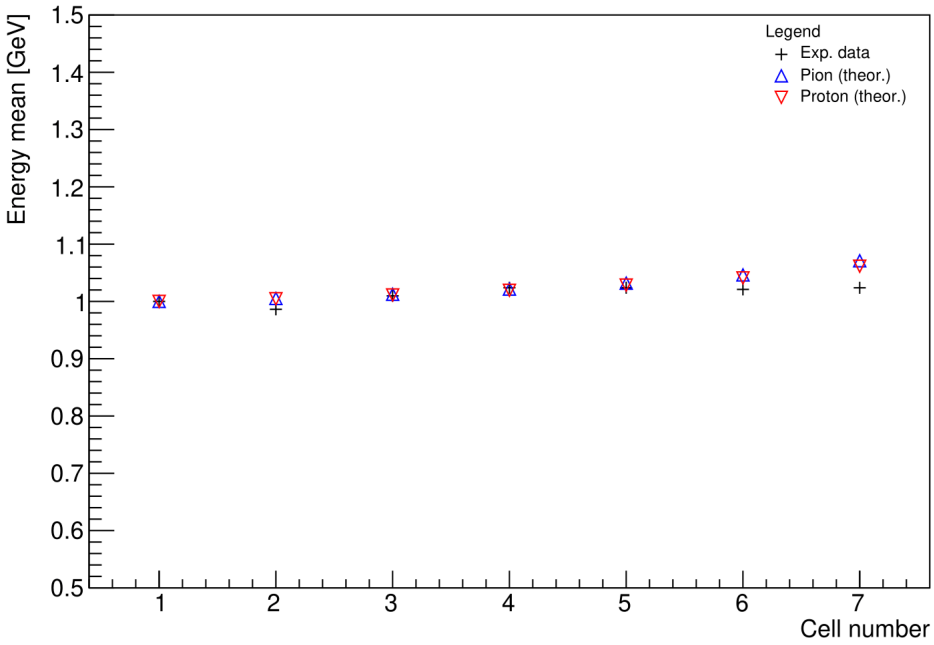

Figure 5.10: Normalized mean energy dependency on the targeted cell.

Conclusion

In this thesis, we performed two separate analyses of TileCal test beam data from November 2018.

In the first part, we carried out a review of electromagnetic calibration constants for extended barrel TileCal module, which are adjusting for the differences in radial response. We investigated the ratio values B/A and D/A which are comparing energy response in B (and D) cell layer to the energy response in A cell layer. As the calibration constants had already been applied, we assumed both of the coefficients B/A and D/A should be equal to one and therefore the energy response should not be dependent on the cell row targeted. We showed a perfect agreement of the D/A ratio with the expectation. In the case of the B/A ratio, we observed a difference of 2 - 4 % from the hypothesis. This uncertainty was explained by not uniform character of tiles in the TileCal module. Altogether, we consider the electromagnetic constants for radial calibration of TileCal to be successfully verified.

In the second analysis, we reviewed the longitudinal hadron shower profile parametrization established in [13]. We confirmed the correctness of the provided parameters for pion shower profile and used a corrected parametrization for proton shower profile, as follows

$$w_{\text{proton}} = 0.676 - 0.0657 \ln(E_{tot}[\text{GeV}]).$$

Implementing the new w_{proton} parametrization in our calculations, we then accomplished to compare theoretical and experimental mean energy values through a range of angles in the projective geometry. We discovered a difference in the absolute values of the mean energy between theoretical and experimental data. However, when examining the tendency of the distribution after normalization, we concluded, the experimental data match the rising tendency of the calculated values for pions and protons. There is one exception (A-2 cell) which can be caused by a faulty readout channel and then at the end of the spectrum, there is an effect of lateral leakage joining.

Bibliography

[1] CERN Official site. https://home.cern/about/who-we-are/our-history, 2020.

[2] CERN Official site. https://home.cern/news/news/accelerators/new-schedule-lhc-and-its-successor, 2019.

[3] ATLAS Collaboration. *Observation of a new particle in the search for the Standard Model Higgs boson with the ATLAS detector at the LHC* http://www.sciencedirect.com/science/article/pii/S037026931200857X, Physics Letters B, 716(1):1-29, 2012.

[4] Rudiger Voss and Amos Breskin, editors. *The CERN Large Hadron Collider: Accelerator and Experiments.* Volume 1: LHC Machine, ALICE, and ATLAS, 2009.

[5] ATLAS Collaboration. https://twiki.cern.ch/twiki/bin/view/AtlasPublic/PublishedTilecalFigures, 2008.

[6] Anderson, K.J. and others. *Calibration of ATLAS Tile Calorimeter at Electromagnetic Scale*, ATL-TILECAL-PUB-2009-001, ATL-COM-TILECAL-2008-016, 2008.

[7] Thomason, J. and Garoby, Roland and Gilardoni, S. and Jenner, L. and Pasternak, J. *Proton driver scenarios at CERN and Rutherford Appleton Laboratory.* Physical Review Special Topics - Accelerators and Beams, volume 6, 2013.

[8] ATLAS Collaboration. https://twiki.cern.ch/twiki/bin/viewauth/Atlas/TileCalTestbeamAnalysis2016, 2016.

[9] CERN Official site. https://home.cern/science/accelerators/super-proton-synchrotron, 2020.

[10] ATLAS Collaboration. *Testbeam studies of production modules of the ATLAS Tile Calorimeter* https://www.sciencedirect.com/science/article/pii/S016890020900792X, Nuclear Instruments and Methods in Physics Research Section A: Accelerators, Spectrometers, Detectors and Associated Equipment, 606(3):362-394, 2009.

[11] Tomáš Davídek. *Instrumentace a kalibrace hadronového kalorimetru ATLAS Tilecal.* https://www.sciencedirect.com/science/article/pii/S016890020900792X, Charles University in Prague, habilitation thesis, 2009.

[12] Luca Fiorini. *Update of 2018 pion data analysis* https://indico.cern.ch/event/856196/contributions/3603467/attachments/1928522/3193395/tiletb-17-10-2019.pdf, 17.10.2019.

[13] ATLAS Collaboration. *Measurement of pion and proton response and longitudinal shower profiles up to 20 nuclear interaction lengths with the ATLAS Tile calorimeter* http://www.sciencedirect.com/science/article/pii/S0168900210001051, Nuclear Instruments and Methods in Physics Research Section A: Accelerators, Spectrometers, Detectors and Associated Equipment, 615(2):158-181, 2010.

[14] Tibor Ženiš and others. *Test beam mapping of TileCal modules* http://zenis.dnp.fmph.uniba.sk/tile.html

[15] Andrea Rodriguez and others. *Test Beam Studies for the ATLAS Tile Calorimeter Upgrade Readout Electronics* https://iopscience.iop.org/article/10.1088/1742-6596/1162/1/012018, Journal of Physics: Conference Series, 1162, 2019.

[16] Particle Data Group (M. Tanabashi and others). *Review of Particle Physics*, Phys. Rev. D, 98(3):452, 2018.

List of Figures

List of Tables